Available online at www.sciencedirect.com
ScienceDirect
Polymer 49 (2008) 1323–1331
polymer
www.elsevier.com/locate/polymer

The three-phase structure of isotactic poly(1-butene)

Maria Laura Di Lorenzo [a,*], Maria Cristina Righetti [b]

[a] Istituto di Chimica e Tecnologia dei Polimeri (CNR), c/o Comprensorio Olivetti, Via Campi Flegrei, 34, 80078 Pozzuoli (NA), Italy
[b] Istituto per i Processi Chimico-Fisici (CNR), Area della Ricerca, Via G. Moruzzi, 1 – 56124 Pisa, Italy

Received 3 December 2007; received in revised form 4 January 2008; accepted 14 January 2008
Available online 19 January 2008

Abstract

A detailed analysis of the three-phase structure of isotactic poly(butene) was conducted by conventional and temperature-modulated calorimetry. The development of the crystalline, mobile amorphous, and rigid amorphous fractions was analyzed as a function of thermal history, upon isothermal and non-isothermal crystallization. It was found that, under the chosen experimental conditions, the amount of rigid amorphous phase (w_{RA}) in PB-1 ranges from $w_{RA} = 0.14$ to 0.23, with higher values formed when the polymer is crystallized at low temperatures or at high cooling rates from the melt. Comparison of total and frequency-dependent reversing heat capacity curves suggested that the rigid amorphous phase of isotactic poly(1-butene) vitrifies after completion of the crystallization process and that its full mobilization takes place at around 50 °C. The exact temperature of complete devitrification is slightly affected by the thermal history of the material. An effort to link the mechanical properties of PB-1 to the three-phase structure was attempted, and a correlation of Young's modulus with the solid fraction at the temperature of analysis, composed of crystalline and rigid amorphous phases, was proposed.

Keywords: Rigid amorphous phase; Isotactic poly(1-butene); Structure–properties' relationship

1. Introduction

Isotactic poly(1-butene) (PB-1) is a thermoplastic polyolefin with outstanding mechanical properties, like high creep resistance, low stiffness, good impact behavior, and excellent elastic recovery. In addition PB-1 is resistant to a high number of chemicals and is very insensitive to environmental stress cracking in a wide melt flow ranges [1,2]. Despite the excellent properties, applications of PB-1 are limited compared to those of the lighter polyolefins like polyethylene and polypropylene, mainly due to the slightly higher cost of the raw polymer and due to the dimensional changes arising from crystal structure transformation, which complicates the production of goods with stable mechanical properties.

Isotactic poly(1-butene) has a very complex polymorphic behavior, since it can crystallize into various crystalline forms, depending on the preparation conditions [2–13]. Melt crystallization usually leads to the tetragonal Form II, characterized by an 11/3 helix conformation [5,9]. This metastable modification slowly transforms into the hexagonal crystalline Form I, in which the crystalline strands adapt to a slightly extended 3/1 helical conformation [5]. The transformation spontaneously and irreversibly occurs over a wide temperature range, at a rate that finds its maximum around room temperature and that is affected by several chemical, physical, and mechanical factors [3]. The structural and dimensional changes induced by the solid-state II–I transformation are accompanied by a considerable enhancement of the mechanical properties such as hardness, tensile strength, and stiffness [1,14,15].

In the past, several studies have been conducted to analyze the relation between structure and properties in semicrystalline PB-1, and in semicrystalline polymers in general. The basic problems that arise in understanding the properties of semicrystalline polymers are related to the description of their structure based on a two-phase model, viewed as a skeleton of thin crystal lamellae intermingled with amorphous material. However, it is known that a number of properties cannot be

* Corresponding author. Tel.: +39 081 8675059; fax: +39 081 8675230.
E-mail address: diloren@ictp.cnr.it (M.L. Di Lorenzo).

0032-3861/$ - see front matter © 2008 Elsevier Ltd. All rights reserved.
doi:10.1016/j.polymer.2008.01.026

interpreted using the two-phase approach. For instance, the heat capacity step at the glass transition (T_g) measured by calorimetry is often smaller than that corresponding to the amount of amorphous fraction [16]. To explain the disagreement between the expected and the quantified values of the amorphous content at T_g, Wunderlich first suggested the existence of two types of amorphous fractions in semicrystalline polymers, characterized by different degrees of decoupling with the crystal structure: in addition to the mobile amorphous fraction (MAF) made of the polymer chains that mobilize at T_g, and to the crystal phase, a third fraction of nanosized dimensions, the rigid amorphous phase (RAF), was introduced [16,17]. The rigid amorphous phase arises from the continuation of the partially crystallized macromolecules across the phase boundaries, as the polymer molecules are much longer than the crystal nanophases. The portions of macromolecules whose mobility is hindered by the near crystalline structures appear on both sides of crystalline lamellae, as probed by ^{13}C solid-state NMR [18–22], X-ray diffraction [21], electron microscopy [19], or Raman spectroscopy [18]. The size of the RAF is estimated to be about 4.0 nm for a crystalline lamellar thickness of 25–30 nm [21–23], but thicknesses as low as 0.2–0.7 nm have also been reported [24]. Devitrification of the rigid amorphous phase usually occurs between the T_g of the unstrained amorphous phase and the melting temperature, but this is not a general rule. Some semicrystalline polymers may have no RAF, or may have an RAF which mobilizes in correspondence of the melting, or even above the melting point [17].

Although the existence of the RAF is demonstrated by experimental evidences, its properties are still under investigations. Details about the chain packing in the RAF are largely not known. For instance, it would be of enormous interest to clarify how the crystallization conditions affect RAF vitrification and mobilization. Only a few studies have been published on the kinetics of formation of the RAF and its devitrification [23,25–28]. For some polymers like poly(3-hydroxybutyrate), polycarbonate and isotactic polystyrene, parallel development of the RAF with crystallinity was detected, whereas only partial formation of the RAF during crystallization was evidenced for syndiotactic polypropylene and poly(ethylene terephthalate) at some particular crystallization temperatures [26–28]. In these studies the concurrent development of the crystal phase and of the rigid amorphous fraction was followed at a single temperature. A new method that allows to simultaneously monitor the development of crystalline, mobile amorphous and rigid amorphous fractions during cooling from the melt was recently presented by Righetti et al. [29]. With this procedure, which permits to determine the evolution of the three nanophases in a wide temperature range, it was found that the rigid amorphous fraction in poly(ethylene terephthalate) starts to vitrify when the crystallization process is almost finished and continues further on cooling to the glass transition of the bulk amorphous phase [29].

Only a few attempts have been performed to correlate the properties of semicrystalline polymers with RAF content. Rastogi et al. [30] analyzed the relation between the mechanical properties and the nanostructure of polyethylene terephthalate, showing that the rigid amorphous content needs to be explicitly taken into account to describe the yield behavior and the loss of crystallinity of PET in uniaxial compression. Lin et al. [31] quantified the differences in oxygen solubility of MAF and RAF in PET, which mainly arises from the different specific volume of the two nanophases, a property that can permit to tailor the barrier properties of PET goods.

To our knowledge, no report on the existence of a rigid amorphous fraction in isotactic poly(1-butene) has been published yet. In this contribution, details about vitrification of the rigid amorphous fraction, in dependence of crystallization conditions, are presented. In addition, a correlation between the nanophase structure and the mechanical properties of PB-1 is suggested.

2. Experimental part

2.1. Materials

Isotactic poly(1-butene) (PB-1) of melt flow rate equal to 0.4 g/10 min (190 °C/2.16 kg) was kindly provided by Basell Polyolefins. The material is a commercial PB-1 grade used for extrusion into pipe for potable hot and cold water distribution applications. It contains some nucleating agents, added to accelerate the Form II–Form I phase transformation.

Before analyses, the sample chips were compression-molded with a Carver Laboratory Press at a temperature of 160 °C for 5 min, without any applied pressure, to allow complete melting. After this period, a pressure of about 50 bar was applied for additional 5 min. In order to obtain compression-molded sheets with different contents of crystalline, mobile amorphous, and rigid amorphous phases, the molten material was cooled to room temperature at various rates, and in some cases annealed immediately after quenching.

2.2. Calorimetry

The thermal properties of compression-molded PB-1 were measured with a Perkin–Elmer Pyris Diamond DSC, equipped with Intracooler II as cooling system. The instrument was calibrated in temperature with high purity standards (indium and cyclohexane) and in energy with heat of fusion of indium. Dry nitrogen was used as purge gas at a rate of 48 ml/min. Each measurement was repeated three times to improve accuracy.

To determine the nanophase content of the compression-molded PB-1 sheets, samples of about 15 mg were heated from −60 to 160 °C at a rate of 20 °C/min. The heat-flow rate raw data were corrected for instrumental asymmetry by subtraction of a baseline, measured under identical conditions as the sample run, including close match of the masses of the aluminum pans. The heat-flow rate data were then converted to specific heat capacities by calibration with sapphire [32].

To analyze the effect of crystallization conditions on RAF formation, isothermal crystallization experiments were performed. The compression-molded PB-1 samples, weighing

about 15 mg, were heated from 25 to 160 °C at a rate of 20 °C/min, melted at 160 °C for 10 min to erase previous thermal history, then cooled at a rate of 50 °C/min to T_c and allowed to crystallize. The isothermally crystallized samples were then cooled from T_c to −60 °C at a rate of 50 °C/min, held at −60 °C for 5 min, and then heated to 160 °C at 20 °C/min. Non-isothermal crystallizations were performed after melting at 160 °C for 10 min, by cooling the samples from 160 to −60 °C at various rates: 2, 5, 10, 20, and 50 °C/min. The material was then maintained at −60 °C for 5 min and heated to 160 °C at 20 °C/min.

Temperature-modulated DSC analyses were conducted on PB-1 samples weighting about 4 mg, using a saw-tooth temperature profile with heating-only modulation segments and various periods (p) of temperature oscillations, ranging from $p = 60$ to 180 s. The underlying heating rate was 2 °C/min. The reversing heat capacity was obtained from the ratio of the first harmonics of the Fourier series that describe the amplitudes of heat flow and temperature. Again, to obtain precise heat capacity data, each measurement was accompanied by an empty pan run and a calibration run with sapphire under identical conditions.

2.3. WAXS analysis

Wide-angle X-ray scattering (WAXS) analysis was carried out on a Philips (PW 1050 model) powder diffractometer (Cu Ni-filtered radiation) equipped with a rotative sample holder device.

2.4. Tensile tests

Dumbbell-shaped specimens were cut from compression-molded sheets subjected to various thermal histories and used for tensile measurements. Stress–strain curves were obtained with an Instron machine (Model 4505) at crosshead speed of 10 mm/min. Data were extracted from an average of seven specimens.

3. Results and discussion

Experimental total specific heat capacity ($c_{p,Tot}$) and frequency-dependent reversing specific heat capacity ($c_{p,Rev}$) of PB-1, measured after isothermal crystallization at 98 °C followed by cooling to −60 °C, are compared in Fig. 1a and b with thermodynamic c_p values of fully solid and liquid PB-1, as taken from the ATHAS Data Bank [33]. The total c_p data reveal a heat capacity step centered at around −28 °C, caused by the glass transition of the MAF, followed by a broad and very weak exotherm, then the experimental c_p remains below the baseline curve of liquid PB-1 until the onset of fusion. Two melting endotherms can be distinguished in the thermogram: a large one at low temperature, due to the fusion of PB-1 crystallites of Form II grown upon crystallization from the melt, and a second smaller one, that reveals the melting of a small portion of Form I crystals, that have converted from the metastable modification II

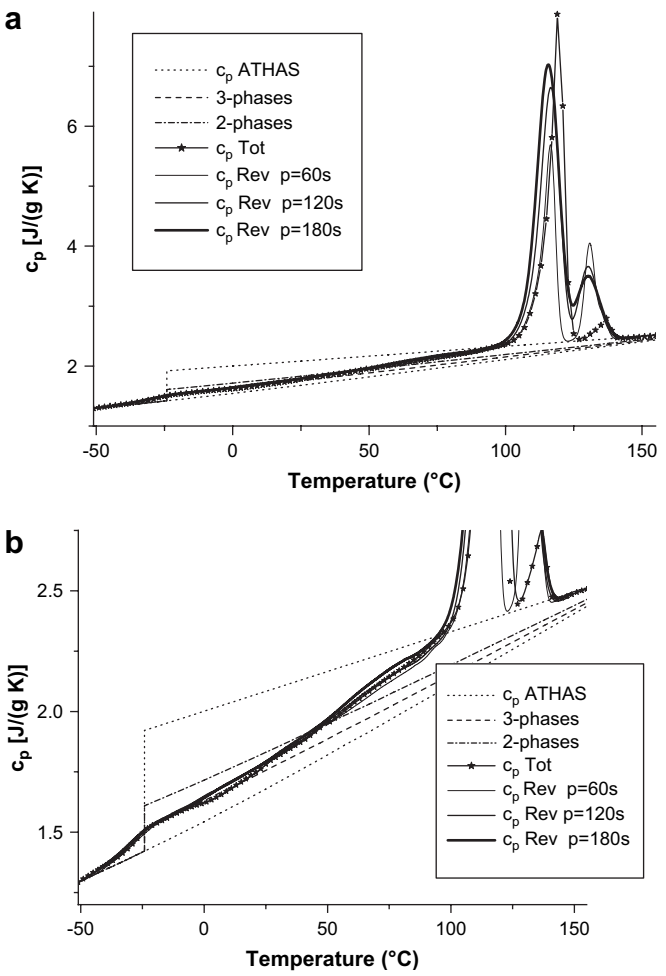

Fig. 1. (a) Specific heat capacity of PB-1 after isothermal crystallization at 98 °C and subsequent cooling to −60 °C. The dotted lines are the solid and liquid specific heat capacities, as taken from the ATHAS Data Bank [33]. (b) Enlargement of the plot in the baseline c_p area. The dashed line is the total specific heat capacity measured by conventional DSC and the solid lines are the reversing specific c_p obtained from TMDSC analysis at the indicated periods of modulation. c_p baselines calculated from the two-phase and three-phase models are also shown.

during the cooling from T_c to −60 °C and during the DSC heating scan, as detailed below. The observation of a small amount of Form I crystals in a PB-1 sample not subjected to aging is to be ascribed to the presence of some nucleating agents in the commercial material that have been added to the formulation in order to accelerate the Form II–Form I phase transition.

Two smaller endotherms are recorded also in the reversing c_p curves derived from TMDSC measurements. The maxima of both endothermic peaks are shifted to slightly lower temperatures with respect to the $c_{p,Tot}$ data, indicating some degree of superheating in the conventional DSC analysis, which arises from the higher heating rate coupled with the larger sample mass, as detailed in Section 2. In addition, the relative positions of the two endotherms in the $c_{p,Tot}$ and $c_{p,Rev}$ plots reveal that PB-1 crystallites do not improve during the slower TMDSC beyond the perfection gained during the conventional DSC analysis.

The experimental data shown in Fig. 1 allow to determine the content of the mobile amorphous, rigid amorphous and crystalline phases. To obtain quantitative data, precise knowledge of thermodynamic values of heat of fusion (Δh) and heat capacity step at T_g (Δc_p) is needed. Unfortunately, the exact melting enthalpies of the ideal crystals of both modifications I and II of PB-1 are not known, as the reported data of heat of fusion of Form I (Δh_I^o) vary in a rather wide interval that extends from 110 to 150 J/g, and the corresponding value for the less stable modification II (Δh_{II}^o) ranges from 60 to 110 J/g [34,35]. A critical analysis of literature data supported by combined DSC and density measurements on a number of samples with different crystallinity degrees, detailed in Ref. [35], suggests 141 ± 10 and 62 ± 3 J/g as the most probable values for the heat of fusion of modifications I and II, respectively. These values were used to calculate the crystal fraction of the isothermally crystallized samples. Contrary to heat of fusion, precise literature data of thermodynamic heat capacity of poly(1-butene) are available and a value of 0.412 J/(g K) is the recommended Δc_p step at T_g in the ATHAS Data Bank, quantified on the basis of three very close literature reports [33,36].

The heat capacity step at T_g after isothermal crystallization at $T_c = 98$ °C and cooling accounts for a mobile amorphous phase content (w_A) of 0.19_1, as illustrated in Fig. 1b, that presents an enlargement of Fig. 1a. On the same plot, the reversing c_p curves are also shown, in order to provide additional details on the small exotherm that appears in the DSC plot of Fig. 1b between −8 and 25 °C. As proven by comparison of the total and reversing c_p plots, this small exothermic event is fully irreversible, and discloses a latent heat exchange equal to 0.260 J/g. The nature of this transition, whether it arises from additional crystallization or from a solid–solid phase transition is not revealed by mere DSC analyses, however, the heat exchanged is very small compared to the major thermal events, being barely distinguishable in Fig. 1a, and its accounting or neglecting in the calculation provides a rather negligible uncertainty in the estimation of the overall crystallinity. In fact, its contribution to overall crystallinity amounts to 0.004 in case it is due to secondary cold crystallization into Form II.

The crystal fraction w_C was quantified both from integration of the exothermic peak evolved during isothermal crystallization and from the endotherms recorded during the heating scans. A close inspection of the heat-flow rate curve recorded after permanence at T_c, during the cooling runs to −60 °C, did not give evidences of further crystallization. Analysis of the heat evolved during isothermal crystallization at 98 °C provides $w_C = 0.62_4$. Integration of the melting peaks was performed using the application of the Pyris software that allows to calculate partial areas of DSC traces. This calculation method provides reliable data only if the endotherms related to fusion of the different type of crystals are well separated and a temperature value at which the intensity of the signal returns to the baseline value can be identified in the melting range, as demonstrated by Alfonso et al. [35]. Such a value can be safely recognized in Fig. 1, as the experimental $c_{p,Tot}$ curve displays a deep minimum between the two main endotherms, because of the very small amount of Form I developed. Integration of the fusion thermograms after proper separation of the different contributions of the two crystal modifications, as detailed above, gives $w_C = w_{cI} + w_{cII} = 0.63_0$, where $w_{cI} = 0.01_7$ is the crystal fraction of Form I and $w_{cII} = 0.61_3$ is the crystal fraction of Form II. Accounting for the small endotherm as a cold crystallization process provides $w_C = 0.62_6$. The crystalline fraction calculated from the endotherms on heating is very close to the w_C content determined form isothermal data. The latter is used for the determination of the nanophase structure after crystallization at $T_c = 98$ °C and subsequent cooling. The content of rigid amorphous phase is quantified by difference using the equation

$$w_C + w_A + w_{RA} = 1 \tag{1}$$

which yields a value of $w_{RA} = 0.18_5$.

Besides the experimental total and reversing c_p, Fig. 1a and b reports the baseline specific heat capacity, that is the heat necessary to increase the temperature of a sample without changes in the nanophase structure, estimated from a three-phase model, as $c_p = w_A c_{p,A} + (w_C + w_{RA}) c_{p,C}$, with $w_A = 0.19_1$, $w_C = 0.62_4$ and $w_{RA} = 0.18_5$, where $c_{p,A}$ and $c_{p,C}$ are the thermodynamic specific heat capacities of solid and liquid PB-1, respectively, as taken from the ATHAS Data Bank [33]. From T_g up to −8 °C, no difference between the reversing c_p and the three-phase baseline is observed, attesting that the relative compositions of the nanophases remain unchanged in this temperature range. At higher temperatures the reversing c_p is significantly higher than the three-phase baseline and at approximately 50 °C crosses the baseline calculated from a two-phase model, as $c_p = (1 - w_C) c_{p,A} + w_C c_{p,C}$, with $w_C = 0.62_4$. The very close overlapping of the reversing c_p plots, which results independent of the frequency of modulation, suggests that between −20 and 50 °C no reversing latent heat is exchanged, and that the increase of the reversing c_p is to be ascribed to thermodynamic effects only. Conversely, above 50 °C the frequency dependence of the $c_{p,Rev}$ plot reveals the occurrence of thermal processes involving reversing exchanges of latent heat [25,26]. In these conditions, the reversing c_p data up to 50 °C correspond to the baseline specific heat capacity. This allows to estimate the temperature dependence of devitrification of the amorphous fraction using the equation [29]

$$w_A(T) = \frac{c_{p,Rev}(T) - c_{p,C}(T)}{c_{p,A}(T) - c_{p,C}(T)} \tag{2}$$

where $c_{p,C}$ and $c_{p,A}$ are the thermodynamic heat capacities of the solid and the liquid PB-1, that are collected in the ATHAS Data Bank [33]. Data were analyzed from above the glass transition of the MAF, in order to determine by difference the evolution with temperature of the rigid amorphous fraction. Results of this analysis, illustrated in Fig. 2, reveal that the RAF of PB-1 starts to gradually mobilize at about 10 °C above the end point of the T_g of the MAF, and that devitrification of the RAF is completed at 49 °C. As shown in Fig. 1b, at this temperature the $c_{p,Rev}$ curves intersect the two-phase baseline, confirming that above 49 °C all the amorphous materials are liquid. PB-1

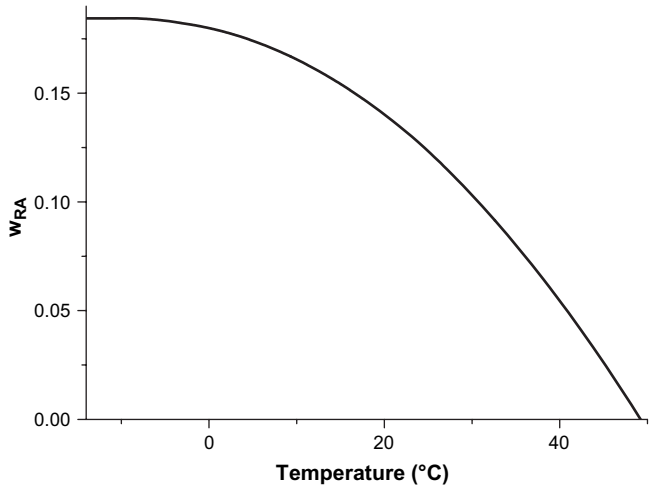

Fig. 2. Rigid amorphous weight fraction (w_{RA}) of PB-1 after isothermal crystallization at $T_c = 98$ °C and cooling to −60 °C as a function of temperature during the subsequent heating at 20 °C/min.

crystals were isothermally grown at $T_c = 98$ °C, far above the temperature of full devitrification of the RAF. This proves that the rigid amorphous fraction of PB-1 does not develop simultaneously with the crystal phase, but only during the cooling to T_g.

Fig. 3a illustrates the specific heat capacity curves of PB-1 after isothermal crystallization at various temperatures followed by cooling to −60 °C. In Fig. 3b, an enlargement of Fig. 3a, showing plot details around the glass transition of the MAF, is presented. All the curves, collected after isothermal crystallization in the range $80 \leq T_c \leq 104$ °C, reveal the presence of both crystal modifications I and II. The amount of modification II increases from $w_{cII} = 0.53_7$ to 0.64_2 when T_c is raised from 80 to 104 °C. Conversely, the fraction of crystals that have converted into Form I during cooling from T_c and/or the heating scan is independent of T_c, being $w_{cI} = 0.017 \pm 0.002$ for all the analyzed T_c range. Hence, the large increase of the crystal fraction with T_c has to be ascribed to augmented amounts of crystallites grown in the metastable modification II. Interestingly, the fusion endotherms of both Form I and Form II move to higher temperatures with increasing T_c. This reveals that the fraction of crystals that changes from Form II to Form I, whose amount remains constant with T_c, has progressively higher thermal stability when crystallization is conducted at high temperatures.

The crystallization temperature affects also the glass transition behavior of poly(1-butene): the specific c_p curves overlap, within experimental errors, from low temperatures until mobilization of the MAF approaches completion, which occurs at a temperature that slightly lowers with T_c. As a consequence, the c_p jump at T_g decreases with the crystallization temperature. Also the shallow and broad exotherm that follows the glass transition is influenced by crystallization conditions, resulting more pronounced at high T_c. However, the latent heat associated to this thermal event is very low, ranging from 0.16_6 to 0.31_3 J/g when T_c is raised from 80 to 104 °C.

The mobile amorphous, rigid amorphous and crystalline fractions after isothermal crystallization and cooling to −60 °C are presented in Fig. 4 as a function of T_c. As before, w_C data

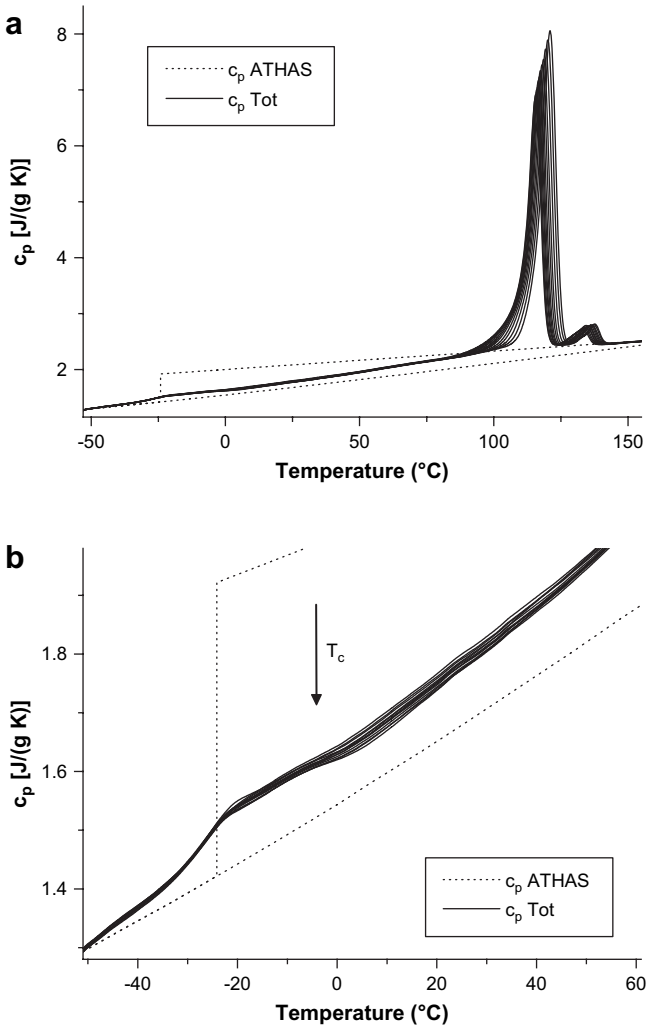

Fig. 3. (a) Specific heat capacity of PB-1 after isothermal crystallization at $80 \leq T_c \leq 104$ °C and subsequent cooling to −60 °C. Data were gained at T_c steps of 2 °C. The dotted lines are the solid and liquid specific heat capacities, as taken from the ATHAS Data Bank [33]. (b) Enlargement of the plot before fusion.

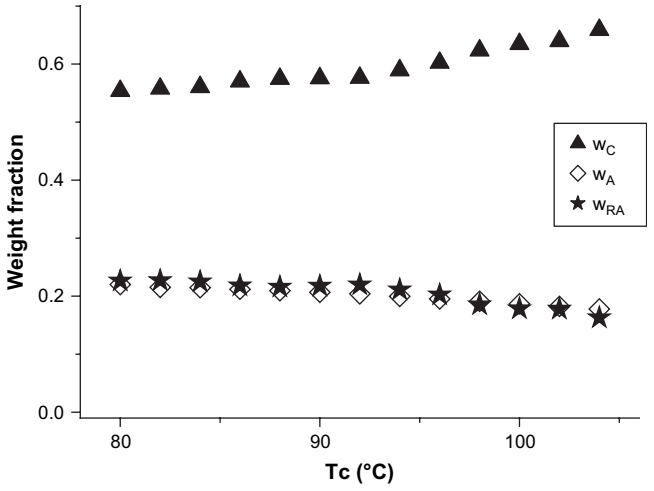

Fig. 4. Crystalline (w_C), mobile amorphous (w_A), and rigid amorphous (w_{RA}) fractions of isotactic poly(1-butene) after isothermal crystallization and subsequent cooling to −60 °C, in dependence of isothermal crystallization temperature (T_c).

were obtained from the crystallization exotherms, the MAF content from the heat capacity step at T_g, and the rigid amorphous fraction by difference, using Eq. (1). An increase in crystallization temperature leads to progressively higher amounts of crystal phase and in a minor decrease of the mobile amorphous phase. The overall effect is that also the rigid amorphous fraction diminishes with T_c, with a larger extent observable at higher crystallization temperatures. The estimated amount of the RAF of PB-1, that ranges from 0.16 to 0.23 for $80 \leq T_c \leq 104$ °C, well compares with that of the lighter polyolefins, which is around 0.20–0.30 for polyethylene and 0.30 for isotactic polypropylene [17]. Devitrification of the RAF, determined with Eq. (2) and the procedure detailed above, starts from above the T_g of the MAF and is completed at a temperature that ranges from 48 to 52 °C, depending on T_c. This reveals a weak influence of the crystallization conditions on mobilization of the RAF. It is worth noting that the data shown in Fig. 4 are slightly affected by the crystallization time at T_c, which adds some errors to the estimation of the three-phase structure of poly(1-butene). For instance, crystallization of PB-1 at 90 °C is completed within 6 min. An increase of the time of permanence (t_c) at $T_c = 90$ °C from 10 to 60 min, which is in the range of the crystallization times used, does not change the MAF ($w_A = 0.20_7$), but leads to progressively slightly higher values of the crystal fraction, equal to 0.57_6, 0.58_1, and 0.58_2 when $t_c = 10$, 30, and 60 min, which correspond to $w_{RA} = 0.21_7$, 0.21_2, and 0.21_1, respectively. However, these variations are below those caused by the changes in crystallization temperature illustrated in Fig. 4.

The T_c dependence of the RAF can be explained by assuming that lower crystallization temperatures result in the formation of thinner lamellae and lower degrees of crystallinity, as also shown in Fig. 4, which correspond to an increased area for localization of strained amorphous chain portions [17]. In addition, crystal growth rates are high at low T_cs, which leads to short time for the adjustment of the crystals into the locally energetically most favorable states. Internal stresses are not released during crystal growth, due also to reduced chain mobility at low temperatures, and concentrate at the interface between the crystal and the amorphous phases, resulting in a large rigid amorphous fraction that vitrifies on cooling. In other words, crystallization at high temperatures increases crystal perfection, with a reduced coupling between crystalline and amorphous structures, that causes a decrease in the amount of RAF and of the local stress at the crystal surfaces. The latter hypothesis is confirmed, as detailed above, by the slight increase of the crystal fraction on prolonged annealing at $T_c = 90$ °C, which occurs at the expense of the rigid amorphous fraction, leaving the amount of mobile amorphous phase unchanged.

Non-isothermal crystallization data of isotactic poly(1-butene) are presented in Fig. 5. Fig. 5a shows the heat-flow rate curves of PB-1 obtained at various cooling rates from the melt. As expected, with increasing the cooling rate (q), the crystallization curves shift to lower temperatures: at low cooling rates there is more time to overcome the nucleation barrier, so crystallization starts at high temperatures, whereas at high rates nuclei become active at low temperatures [37]. The shift of the crystallization exotherms with cooling rate allows to extend the T_c range to lower temperatures compared to the isothermal experiments. The specific heat capacity curves of PB-1 gained after non-isothermal crystallization at various rates are illustrated in Fig. 5b and enlarged in Fig. 5c to show plot details around the baseline c_p. Some light enthalpy relaxation of the MAF is visible in the curves obtained after crystallization at low cooling rates, due to the prolonged annealing below T_g. Besides this small enthalpic effect, in the glass transition area all the curves almost overlap within experimental errors, indicating that, in the range of the analyzed crystallization conditions, the cooling rate from the melt has a very weak influence on the amount of mobile amorphous phase that vitrifies upon cooling. This is in good agreement with the data reported in Fig. 4, upon comparison of the T_c range covered by the isothermal and non-isothermal crystallization experiments. A variation of the cooling rate from the melt affects the amount of crystal phase that develops in PB-1. Low cooling rates favor an increase of the crystal fraction not only of Form II, but also of Form I, due to the prolonged permanence at temperatures where the transformation II–I occurs at maximum rate.

From the w_C and w_A data, the amount of rigid amorphous phase was calculated using Eq. (1). It was found that the RAF that vitrifies on cooling increases with the scanning rate, which corresponds to faster crystallization conditions leading to higher degrees of coupling of the phases, as detailed above. The temperature at which the RAF achieves complete mobilization is located at around 50 °C, with some minor influence of the cooling rate, as seen in Fig. 5c from intersection of the experimental data with the baseline c_p obtained from the two-phase model. The overall effect of non-isothermal crystallization on the three-phase structure of poly(1-butene) is summarized in Fig. 6. It is interesting to note that, under the chosen experimental conditions, the crystalline, mobile amorphous and rigid amorphous fractions display an almost linear trend when plotted vs. the logarithm of cooling rate.

Once established that by varying the cooling conditions it is possible to tailor the nanophase structure of PB-1, a number of compression-molded samples containing different ratio of crystalline, mobile amorphous and rigid amorphous phases were prepared by following different cooling paths from the melt. A few samples were also annealed to increase the range of variation of the three nanophases. Before determination of the mechanical properties, all the samples were stored at room temperature to allow completion of the Form II–Form I phase transition, which was verified by calorimetry and confirmed by X-ray diffraction analysis. The tensile stress–strain behavior of the compression-molded samples was analyzed at 25 °C. Fig. 7 reports Young's modulus (E) of PB-1 as a function of crystal fraction. Some increase of the modulus with crystallinity can be seen in Fig. 7, however, the experimental data are rather scattered. Linear fit of the data results in a correlation factor (R) equal to $R = 0.968$, and a standard deviation (SD) of 0.90. The glass transition of the mobile amorphous

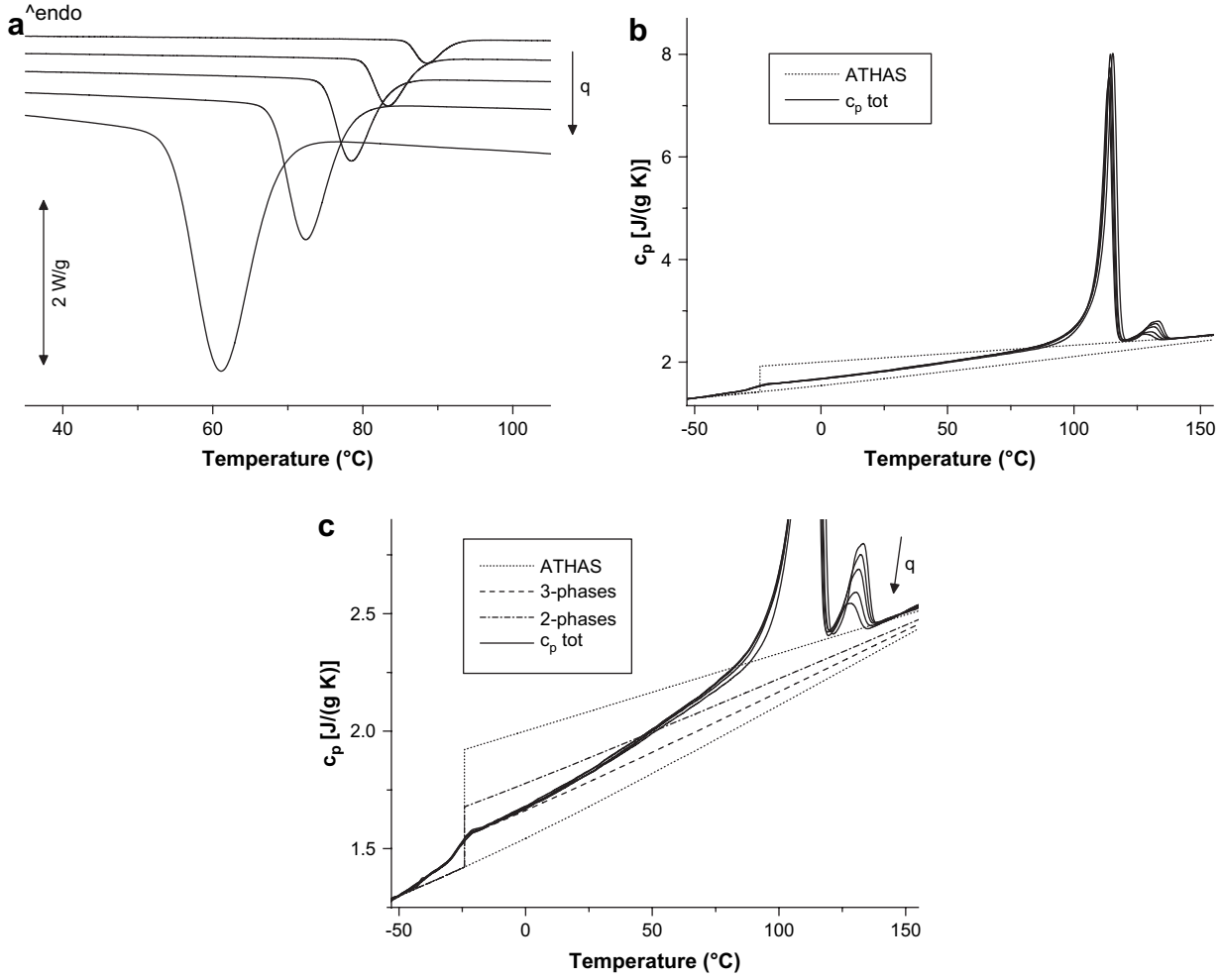

Fig. 5. (a) DSC thermograms of PB-1 crystallized from the melt at various rates $q = 2$, 5, 10, 20, 50 °C/min. (b) Specific heat capacity of PB-1 after non-isothermal crystallization at $q = 2$, 5, 10, 20, 50 °C/min. The dotted lines are the solid and liquid specific heat capacities, as available from the ATHAS Data Bank [33]. (c) Enlargement of Fig. 5b in the baseline c_p area. c_p baselines calculated for the data obtained after crystallization at 20 °C/min from the two-phase and three-phase models are also shown.

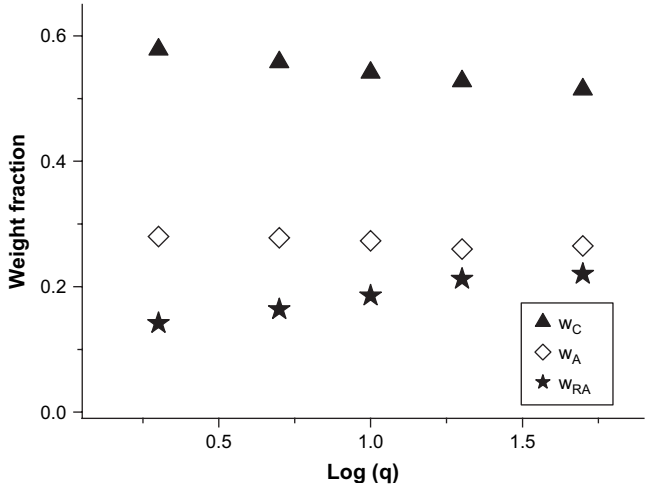

Fig. 6. Crystalline (w_C), mobile amorphous (w_A), and rigid amorphous (w_{RA}) fractions of isotactic poly(1-butene) after non-isothermal crystallization plotted as a function of the logarithm of cooling rate from the melt (q).

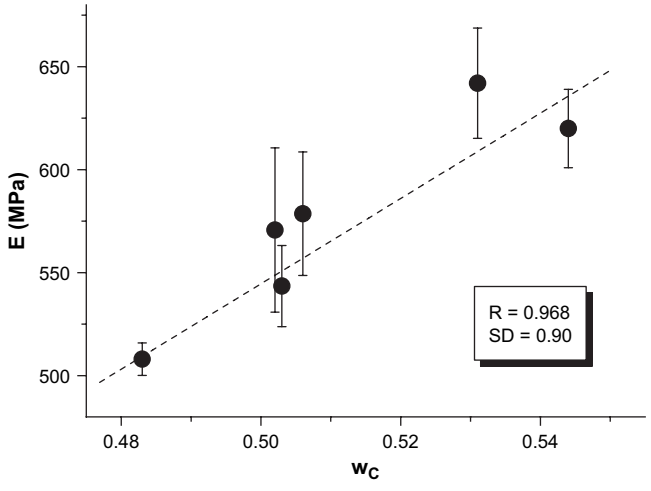

Fig. 7. Young's modulus (E) at 25 °C plotted as a function of the crystal fraction (w_C) of compression-molded PB-1 samples. The dashed line is the linear fit of the experimental data. The correlation factor (R) and the standard deviation (SD) of the linear fit are also displayed.

Table 1
Nanophases' content at 25 °C in the PB-1 samples used for the tensile stress–strain analyses

Sample	w_A	w_C	w_{RA}	w_R
1	0.24_0	0.53_1	0.22_9	0.76_0
2	0.31_2	0.50_3	0.18_5	0.68_8
3	0.35_2	0.48_3	0.16_5	0.64_8
4	0.29_4	0.50_2	0.20_4	0.70_6
5	0.26_4	0.50_6	0.23_0	0.73_6
6	0.24_8	0.54_4	0.20_8	0.75_2

phase of PB-1 is located at −28 °C, as detailed above. From the calorimetric data it was hypothesized that complete devitrification of the RAF of PB-1 occurs at around 50 °C. Hence, at room temperature, where the tensile stress–strain experiments were conducted, the PB-1 samples present a crystalline phase, a mobile amorphous phase, and a partially vitrified rigid amorphous phase. It may be reasonable to report the physical parameters of isotactic poly(1-butene) not only as a function of crystallinity, but also in terms of an overall rigid fraction (w_R), that comprises both the crystal and the vitrified rigid amorphous phases ($w_R = w_C + w_{RA}$). The overall fraction of amorphous material that is mobilized at $T = 25$ °C is calculated using Eq. (2). The amounts of the three nanophases and the overall rigid fraction at $T = 25$ °C in the PB-1 samples used for the tensile experiments are summarized in Table 1.

The w_R dependence of Young's modulus is presented in Fig. 8. A much better correlation of the experimental data can be observed in Fig. 8, compared to the data shown in Fig. 7, where Young's modulus is plotted as a function of the crystal fraction only. This is also probed by the higher value of the correlation factor $R = 0.990$ of the linear fit, closer to 1, and by the lower standard deviation of the data SD = 0.51, compared to the plot shown in Fig. 7.

As mentioned in Section 1, mechanical properties of semicrystalline polymers are usually described in terms of a two-phase model, where each phase is assumed to have intrinsic properties. In an unoriented polymer the phases are randomly mixed and differences in the observed properties result from the relative amounts of the two phases. There are suggestions in the literature that the elastic modulus is a linear function of crystallinity, as reported for a number of polymers, like polyethylene, isotactic polypropylene, polystyrene, or nylons, to cite a few [38–42], although largely scattered E vs. w_C data also appeared in the literature [43]. The monotonic dependence of Young's modulus with crystallinity is generally explained by taking into account the much larger modulus of the crystal phase compared to that of the mobile amorphous phase, the difference amounting to three decades [42]. However, from comparison of Figs. 7 and 8, it seems reasonable to rationalize low strain material properties according to a three-phase model, by explicitly taking into account the contribution of the rigid amorphous phase. If it is assumed that the modulus of vitrified RAF is equal to that of the crystal phase, a linear relationship between Young's modulus and the rigid content of the material ($w_C + w_{RA}$) is expected. The closely linear trend of the data exhibited in Fig. 8 appears to confirm this hypothesis.

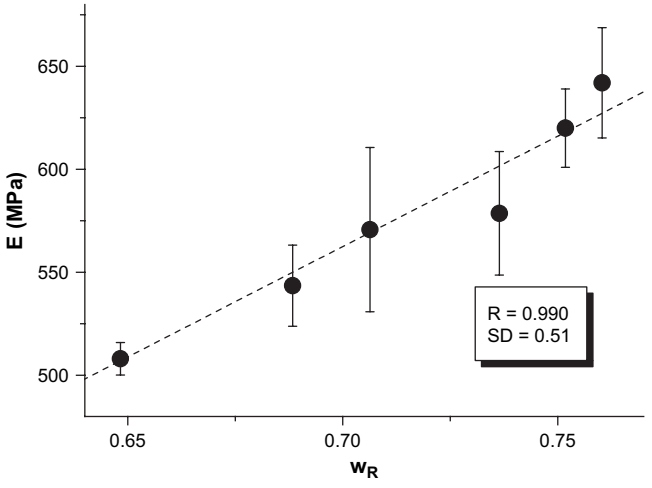

Fig. 8. Young's modulus (E) at 25 °C of the compression-molded PB-1 samples plotted as a function of the rigid fraction ($w_R = w_C + w_{RA}$) at 25 °C. The dashed line is the linear fit of the experimental data. The correlation factor (R) and the standard deviation (SD) of the linear fit are also displayed.

The elastic modulus of a semicrystalline polymer seems not determined only by the degree of crystallinity, as also noted in Ref. [43]. Besides the variations in crystal fraction, differences in the interlamellar amorphous layers produce corresponding changes in entanglement concentration, degree of chain span and number of tie molecules bridging the neighboring crystals. Hence the response of a solidified polymer to strain needs to be linked to the role that the amorphous phase plays in transmitting the load to the crystals and accommodating the initial elastic strain. If the amorphous and crystalline phases are largely coupled, as occurs in isotactic poly(1-butene), an influence of the rigid amorphous phase on the material's mechanical response is expected, due to its localization at the interface between the two other nanophases.

4. Conclusions

Isothermal and non-isothermal DSC analyses revealed that isotactic poly(1-butene), similarly to other semicrystalline polymers, is characterized by a three-phase structure, composed of crystalline, mobile amorphous and rigid amorphous fractions. The relative amounts of the three nanophases depend on the characteristics of the amorphous layers, which vary according to the thermal history of the material. Fast crystallization conditions, attained at low temperatures and/or high cooling rates from the melt, favor the formation of large amounts of the RAF, which starts to vitrify only after completion of crystallization. The amorphous and crystalline phases in PB-1 are largely coupled, with points of coupling lying on the boundary between the phases. These act as nanoscopic stress transfer, with remarkable effects on mechanical properties of the material. Hence, for a complete description of the mechanical behavior, it is necessary to account for the role played by all the three nanophases. This is expected to hold not only for isotactic poly(1-butene), but also for other semicrystalline polymers containing considerable amounts of rigid amorphous phase.

Acknowledgements

The authors express their gratitude to Dr. Vincenzo Frezza of ICTP-CNR for his valuable assistance with WAXS experiments and data analysis, as well as to Dr. Gilberto Moscardi of Basell Poleolefins for kindly providing the PB-1 sample.

M.L.D.L. (ICTP-CNR) gratefully acknowledges the financial support received by Italian Ministero dell'Istruzione dell'Università e della Ricerca (MIUR), D.D. 9-10-02, prot. n. 1105/2002.

References

[1] Luciani L, Seppala J, Logfren B. Prog Polym Sci 1988;13:37–62.
[2] Basell Polyolefins web site: www.basell.com.
[3] Azzurri F, Gómez MA, Alfonso GC, Ellis G, Marco C. J Macromol Sci Phys 2004;B4:3177–89.
[4] Natta G, Corradini P, Danusso F, Mantica E, Mazzanti G, Pino P, et al. J Am Chem Soc 1955;77:1708–10.
[5] Natta G, Corradini P, Bassi IW. Nuovo Cimento 1960;15:52–67.
[6] Miller RL, Holland VH. J Polym Sci Part B Polym Lett 1964;2:519–21.
[7] Danusso F, Gianotti G. Die Makromol Chem 1965;88:149–58.
[8] Cojazzi G, Malta V, Celotti G, Zanetti R. Die Makromol Chem 1976; 177:915–26.
[9] Petraccone V, Pirozzi B, Frasci A, Corradini P. Eur Polym J 1976; 12:323–7.
[10] Nakafuku C, Miyaki T. Polymer 1983;24:141–8.
[11] Dorset DL, McCourt MP, Kopp S, Wittman JC, Lotz B. Acta Crystallogr Sect B 1994;50:201–8.
[12] Nakamura K, Aoike K, Usaka K, Kanamoto T. Macromolecules 1999; 32:4975–82.
[13] Kaszonyova M, Rybnikar F, Geil PH. J Macromol Sci Phys 2005; B44:377–96.
[14] Azzurri F, Flores A, Alfonso GC, Baltá-Calleja FJ. Macromolecules 2002;35:9069–73.
[15] Azzurri F, Flores A, Alfonso GC, Sics I, Hsiao BS, Baltá-Calleja FJ. Polymer 2003;44:1641–5.
[16] Suzuki H, Grebowicz J, Wunderlich B. Makromol Chem 1985;186:1109.
[17] Wunderlich B. Prog Polym Sci 2003;28:383–450.
[18] Kitamaru R, Horii F, Murayama K. Macromolecules 1986;19:636–43.
[19] Kunz M, Möller M, Heinrich UR, Cantow HJ. Makromol Chem Macromol Symp 1988;20/21:147–58, 1989;23:57–72.
[20] Gabriels W, Gaur HA, Feyen FC, Weeman WS. Macromolecules 1994; 27:5811–20.
[21] Cheng J, Fone M, Reddy VN, Schwartz KB, Fisher HP, Wunderlich B. J Polym Sci Part B Polym Phys 1994;32:2683–93.
[22] Litvinov VM, Mathot VBF. Solid State Nucl Magn Reson 2002;22: 218–34.
[23] Alsleben M, Schick C. Thermochim Acta 1994;238:203–7.
[24] Mandelkern L, Alamo RG, Kennedy MA. Macromolecules 1990; 23:4721–3.
[25] Schick C, Wurm A, Mohammed A. Colloid Polym Sci 2001;279:800–6.
[26] Schick C, Wurm A, Mohammed A. Thermochim Acta 2003;396:119–32.
[27] Xu H, Ince S, Cebe P. J Polym Sci Part B Polym Phys 2003;41:3026–36.
[28] Androsch R, Wunderlich B. Polymer 2005;46:12556–66.
[29] Righetti MC, Tombari E, Angiuli M, Di Lorenzo ML. Thermochim Acta 2007;462:15–24.
[30] Rastogi R, Wellinga WP, Rastogi S, Schick C, Meijer HEH. J Polym Sci Part B Polym Phys 2004;42:2092–106.
[31] Lin J, Shenogin S, Nazarenko S. Polymer 2002;43:4733–43.
[32] Archer DG. J Phys Chem Ref Data 1993;22:1441–53.
[33] Pyda M, editor. ATHAS Data Bank, web address: http://www.prz.rzeszow.pl/athas/databank/intro.html.
[34] Silvestre C, Di Lorenzo ML, Di Pace E. Crystallization of polyolefins. In: Vasile C, editor. Handbook of polyolefins. New York: Marcel Dekker, Inc; 2000. p. 223–48 [chapter 9].
[35] Alfonso GC, Azzurri F, Castellano M. J Therm Anal Calorim 2001; 66:197–207.
[36] Gaur U, Wunderlich BB, Wunderlich B. J Phys Chem Ref Data 1983; 12:29–63.
[37] Di Lorenzo ML. Prog Polym Sci 2003;28:663–89.
[38] Starkweather Jr HW, Moore GE, Hansen JE, Roder TM, Broks RE. J Polym Sci 1956;521:189–204.
[39] Wijga PWO. Physical properties of polymers, monograph no. 5. Soc Chem Ind. New York: McMillan and Co; 1959. p. 35.
[40] Nielsen LA. Mechanical properties of polymers. New York: Reinhold Publishing Co; 1962. p. 116.
[41] Peacock AJ, Mandelkern L. J Polym Sci Part B Polym Phys 1990; 28:1917–41.
[42] Wakabayashi K, Register RA. Polymer 2005;46:8838–45.
[43] Galeski A. Prog Polym Sci 2003;28:1643–99.